



UNIVERSIDADE ESTADUAL DE CAMPINAS
SISTEMA DE BIBLIOTECAS DA UNICAMP
REPOSITÓRIO DA PRODUÇÃO CIENTÍFICA E INTELLECTUAL DA UNICAMP

Versão do arquivo anexado / Version of attached file:

Versão do Editor / Published Version

Mais informações no site da editora / Further information on publisher's website:

<https://www.sciencedirect.com/science/article/pii/S0968089623004091>

DOI: <https://doi.org/10.1016/j.bmc.2023.117561>

Direitos autorais / Publisher's copyright statement:

©2023 by Elsevier. All rights reserved.

DIRETORIA DE TRATAMENTO DA INFORMAÇÃO

Cidade Universitária Zeferino Vaz Barão Geraldo

CEP 13083-970 – Campinas SP

Fone: (19) 3521-6493

<http://www.repositorio.unicamp.br>



Discovery of pyrazolo[3,4-*d*]pyrimidines as novel mitogen-activated protein kinase kinase 3 (MKK3) inhibitors

Jéssica E. Takarada^{a,1,2}, Micael R. Cunha^{a,1}, Vitor M. Almeida^{a,1,3}, Stanley N.S. Vasconcelos^{a,4}, André S. Santiago^a, Paulo H. Godoi^a, Anita Salmazo^{a,5}, Priscila Z. Ramos^a, Angela M. Fala^{a,6}, Lucas R. de Souza^a, Italo E.P. Da Silva^{a,b}, Mario H. Bengtson^{a,b}, Katlin B. Massirer^a, Rafael M. Couñago^{a,c,*}

^a Center of Medicinal Chemistry (CQMED), Center for Molecular Biology and Genetic Engineering (CBMEG), University of Campinas, Av. Dr. André Tosello 550, 13083-886 Campinas, Brazil

^b Department of Biochemistry and Tissue Biology, Institute of Biology, University of Campinas (UNICAMP), Campinas, SP 13083-862, Brazil

^c Structural Genomics Consortium and Division of Chemical Biology and Medicinal Chemistry, UNC Eshelman School of Pharmacy, University of North Carolina, Chapel Hill, NC 27599, United States

ARTICLE INFO

Keywords:

Protein kinase
Kinase inhibitors
Bioluminescence resonance energy transfer (BRET)
Molecular docking

ABSTRACT

The dual-specificity protein kinase MKK3 has been implicated in tumor cell proliferation and survival, yet its precise role in cancer remains inconclusive. A critical step in elucidating the kinase's involvement in disease biology is the identification of potent, cell-permeable kinase inhibitors. Presently, MKK3 lacks a dedicated tool compound for these purposes, along with validated methods for the facile screening, identification, and optimization of inhibitors. In this study, we have developed a TR-FRET-based enzymatic assay for the detection of MKK3 activity *in vitro* and a BRET-based assay to assess ligand binding to this enzyme within intact human cells. These assays were instrumental in identifying hit compounds against MKK3 that share a common chemical scaffold, sourced from a library of bioactive kinase inhibitors. Initial hits were subsequently expanded through the synthesis of novel analogs. The resulting structure–activity relationship (SAR) was rationalized using molecular dynamics simulations against a homology model of MKK3. We expect our findings to expedite the development of novel, potent, selective, and bioactive inhibitors, thus facilitating investigations into MKK3's role in various cancers.

1. Introduction

Mitogen-Activated Protein Kinase Kinase 3 (MKK3), also known as MAP2K3, is a dual-specificity protein kinase that participates in the Mitogen-Activated Protein Kinase (MAPK) pathway.¹ MKK3 becomes

activated through phosphorylation at residues S189 and T193 by upstream protein kinases in this pathway.² Once activated, MKK3 serves as a direct activator of other protein kinases within the MAP kinase pathway, notably the p38 MAP kinases, which, in turn, phosphorylate various downstream targets including transcription factors,

Abbreviations: ATP, Adenosine Triphosphate; BRET, Bioluminescence Resonance Energy Transfer; HTRF, Homogeneous Time Resolved Fluorescence; MKK3, Mitogen-Activated Protein Kinase Kinase 3; TR-FRET, Time-Resolved Fluorescence Resonance Energy Transfer.

* Corresponding author at: Center of Medicinal Chemistry (CQMED), Center for Molecular Biology and Genetic Engineering (CBMEG), University of Campinas, Av. Dr. André Tosello 550, 13083-886 Campinas, Brazil.

E-mail address: rafael.counago@unc.edu (R.M. Couñago).

¹ These authors contributed equally to this work.

² Phenotypic Screening Platform, Microbiology Department, Institute of Biomedical Sciences, University of São Paulo, Av. Prof. Lineu Prestes 1374, 05508-000 São Paulo, Brazil

³ Eurofarma Laboratório S/A, Rodovia Presidente Castello Branco, 3565, 06696-000 Itapevi, Brazil.

⁴ Department of Chemistry and Biology, Toronto Metropolitan University, Toronto, ON 5B 2K3M, Canada.

⁵ Institute of Science and Technology Austria, 3400 Klosterneuburg, Austria.

⁶ Institut für Lebensmittelchemie, University of Hannover, 5 Callinstrasse, 30167, Germany.

<https://doi.org/10.1016/j.bmc.2023.117561>

Received 14 October 2023; Received in revised form 6 December 2023; Accepted 17 December 2023

Available online 20 December 2023

0968-0896/© 2023 The Authors. Published by Elsevier Ltd. This is an open access article under the CC BY-NC license (<http://creativecommons.org/licenses/by-nc/4.0/>).

phospholipases, and other protein kinases.^{3,4}

Within the MAPK pathway, p38 MAP kinases play a central role in regulating diverse cellular processes, such as inflammation, cell growth, and apoptosis. Dysregulation of the p38 MAPK pathway has been linked to various diseases, including psoriasis, Crohn's disease, and cancer.⁵ Consequently, substantial efforts have been devoted to the development of potent p38 MAPK inhibitors.^{6,7} Despite numerous small molecule inhibitors of P38 MAP kinases in clinical trials, no FDA-approved p38 inhibitors are currently in clinical use. This lack of success is often attributed to systemic side effects, likely resulting from both on- and off-target effects.^{8,9} In this context, the pursuit of small-molecule inhibitors that selectively target an upstream MAPK kinase, such as MKK3, presents an attractive therapeutic strategy.¹⁰

Recent studies have highlighted MKK3 as a promising new target for cancer therapy.^{11,12} Silencing of endogenous MKK3 has been shown to impede cell proliferation and tumor survival in cancer cells, while sparing normal cells.¹³ Additionally, combining MKK3 depletion with chemotherapy agents has been shown to reduce clonogenicity and enhanced anti-tumor effects in xenograft tumor models compared to the chemotherapy treatment alone.¹⁴

Despite the increasing evidence of MKK3's involvement in cancer, only a few examples of small-molecule MKK3 inhibitors have been reported to date.¹⁵ The scarcity of MKK3 inhibitors may, in part, be attributed to the absence of robust and facile biochemical and in-cell assays for compound identification, optimization and characterization.

In this study, we present the development of a non-radiometric TR-FRET-based enzymatic assay and an in-cell BRET-based target engagement assay to evaluate the potency of compounds against MKK3. Using

these assays, we have identified pyrazolo-pyrimidines as a class of MKK3 inhibitors. Furthermore, an exploratory structure-activity relationship (SAR) of the pyrazolo-pyrimidines has led to the identification of a novel, cell permeable MKK3 inhibitor. We anticipate that our findings will facilitate the development of more potent and selective inhibitors to investigate the modulation of MKK3 in both normal and disease biology.

2. Results and discussion

2.1. Establishment of a TR-FRET assay for MKK3

To facilitate the discovery of novel MKK3 inhibitors, we sought to establish a homogeneous, TR-FRET-based (HTRF) enzymatic assay using in-house produced enzyme and commercially available reagents. To overcome the need to post-translationally activate MKK3 via co-expression or treatment with MKK3 activating kinases (such as MLK3),¹⁶ we employed a baculovirus system to recombinantly produce a previously described, constitutively-active version of this enzyme having two phosphomimetic mutations (S189E and T193E, hereafter called MKK3E)¹⁷ in insect cells (Fig. 1A; Fig. S1).

To date, reported assay for measuring MKK3 activity *in vitro* have employed an inactive mutant of p38 α as substrate.^{18,19} To circumvent the necessity of recombinantly producing (or commercially acquiring) p38 α , we explored alternative substrates for MKK3E. To achieve this, we assessed the activity of purified MKK3E towards three commercially available synthetic peptides within the HTRF® KinEASE™ STK kit (Cisbio Bioassay). Our results indicated that recombinant MKK3E could phosphorylate all peptide substrates (Fig. S2). Subsequent work was

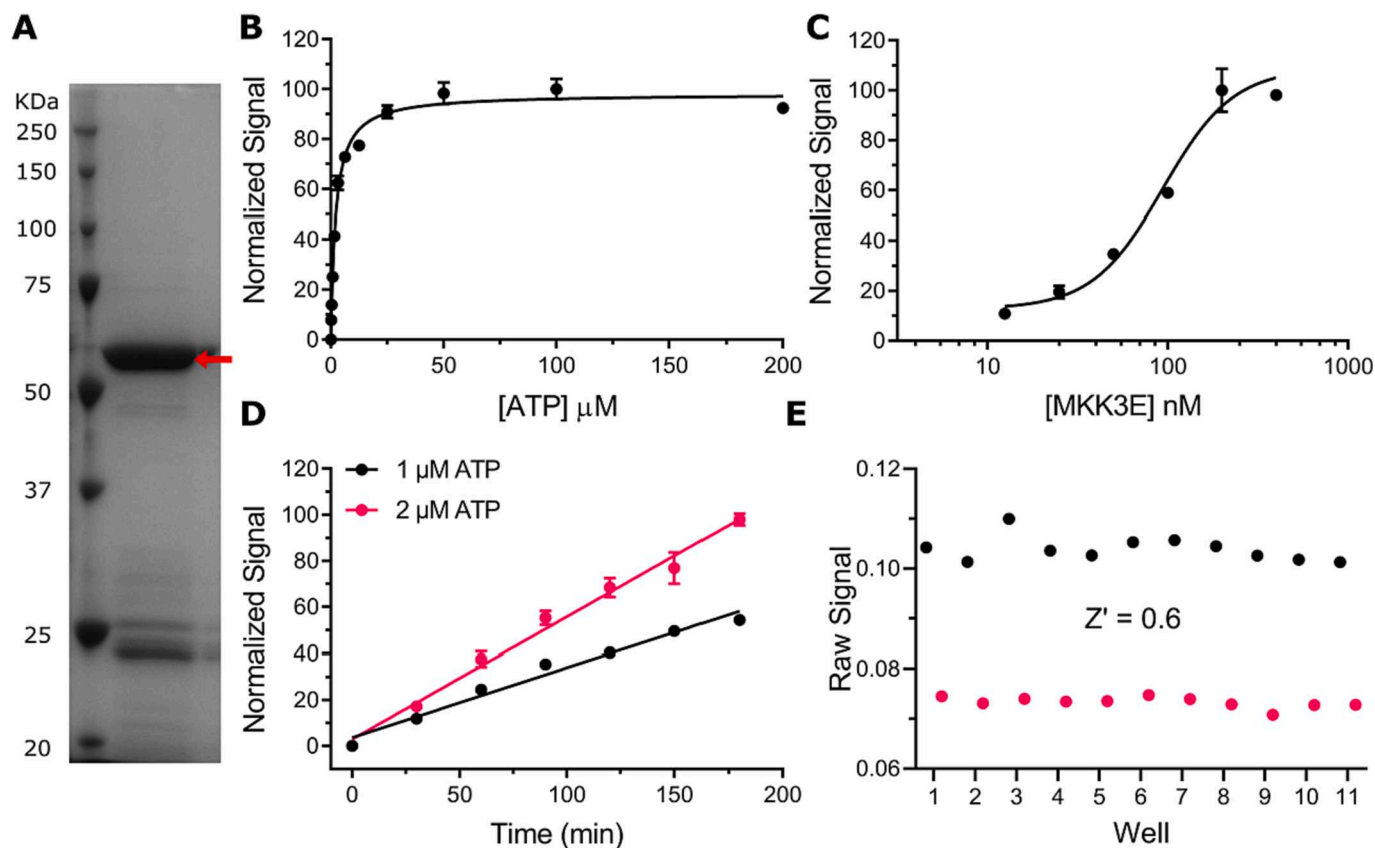


Fig. 1. Production and enzymatic activity characterization of MKK3E: (A) SDS-PAGE displaying purified MKK3E tagged with GST (60 kDa band indicated by a red arrow) after affinity purification using Glutathione Sepharose (red arrow). (B) Determination of $K_{M,ATP}$ for MKK3E. (C) Enzyme titration to establish the optimal protein concentration for subsequent enzymatic assays. (D) Enzyme kinetics at two ATP concentrations, showing linear reaction velocity rates throughout all tested time points. (E) Determination of the Z'-Factor (red circles 0% activity, black circles 100% activity). The raw signal represents the ratio of the fluorescence intensities measured at 665 nm (acceptor emission) and 620 nm (donor emission). All MKK3 reactions were performed at 30 °C. (For interpretation of the references to colour in this figure legend, the reader is referred to the web version of this article.)

performed using substrate STK3.

Using the in-house produced MKK3E and Cisbio TR-FRET reagents, we established a robust and sensitive assay for measuring MKK3E enzymatic activity. Through this assay, we determined the $K_{M,ATP}$ for MKK3E to be 2.1 μM (CI 95 %: 1.8–2.5) (Fig. 1B). While $K_{M,ATP}$ values for MKK3 have not been reported before, the value obtained here was consistent with those commonly observed for other protein kinases, including a constitutively-active, phosphomimetic double mutant of the related MAPK pathway kinase MKK6 (3.6 μM).²⁰ To optimize the assay, we performed an enzyme titration and obtained an EC_{50} value of 95 nM (Fig. 1C). Lastly, a time-course analysis performed with a fixed concentration of MKK3E (100 nM) and either 1 or 2 μM of ATP confirmed that, under these conditions, the amount of phosphorylated peptide increased linearly with reaction time (Fig. 1D). Based on these results, all subsequent enzymatic assays were performed for one hour at 30 °C using 100 nM MKK3E and 1.0 μM ATP. Under these conditions, we estimated a Z' -factor ≥ 0.5 , indicative of a high-quality assay suitable for high-throughput screening (Fig. 1E).²¹

2.2. Development of an in-cell, BRET-based target engagement assay for MKK3

An essential step in early-stage drug discovery programs is the validation of whether selected hits effectively engage the intended target within whole, living cells. An in-cell target engagement assay assesses the compound's capability to permeate cells and interact with the target

within the cellular environment. This is especially pertinent in kinase drug discovery programs since the majority of kinase inhibitors bind to the enzyme's ATP-binding pocket, and cellular ATP concentrations may significantly surpass the ATP K_m for the kinase.²²

A commonly employed strategy to evaluate in-cell target engagement is based on Bioluminescence Resonance Energy Transfer (BRET) between a pair of BRET donor and acceptor molecules.^{23,24} In this assay, the BRET donor comprises the protein of interest (in this case, MKK3) fused to nanoluciferase (Nluc), a small (19 kDa), engineered bioluminescent protein.²⁵ BRET acceptors can be either commercially available or custom-made using fluorescent versions of known target ligands.²⁶ When the BRET acceptor, also referred to as the *tracer*, binds to the Nluc-fused target, the bioluminescent energy from the Nluc reaction is transferred to the tracer fluorophore, resulting in measurable fluorescence at a different wavelength. In competition assays, ligands may be applied exogenously to the system to displace the tracer from the target protein and disrupt the BRET signal.^{23,26}

A significant advantage of establishing a BRET-based, in-cell target engagement assay for MKK3 is that it allows for the identification and evaluation of those cell-permeable compounds capable of effectively outcompeting cellular ATP to engage the kinase. However, it is worth noting that no commercially available tracers have been previously demonstrated to bind to MKK3.

To investigate the potential of commercially available tracers to bind to full-length wild-type MKK3 within cells, we transiently expressed Nluc-fused MKK3 in human (HEK293T) cells and measured the BRET

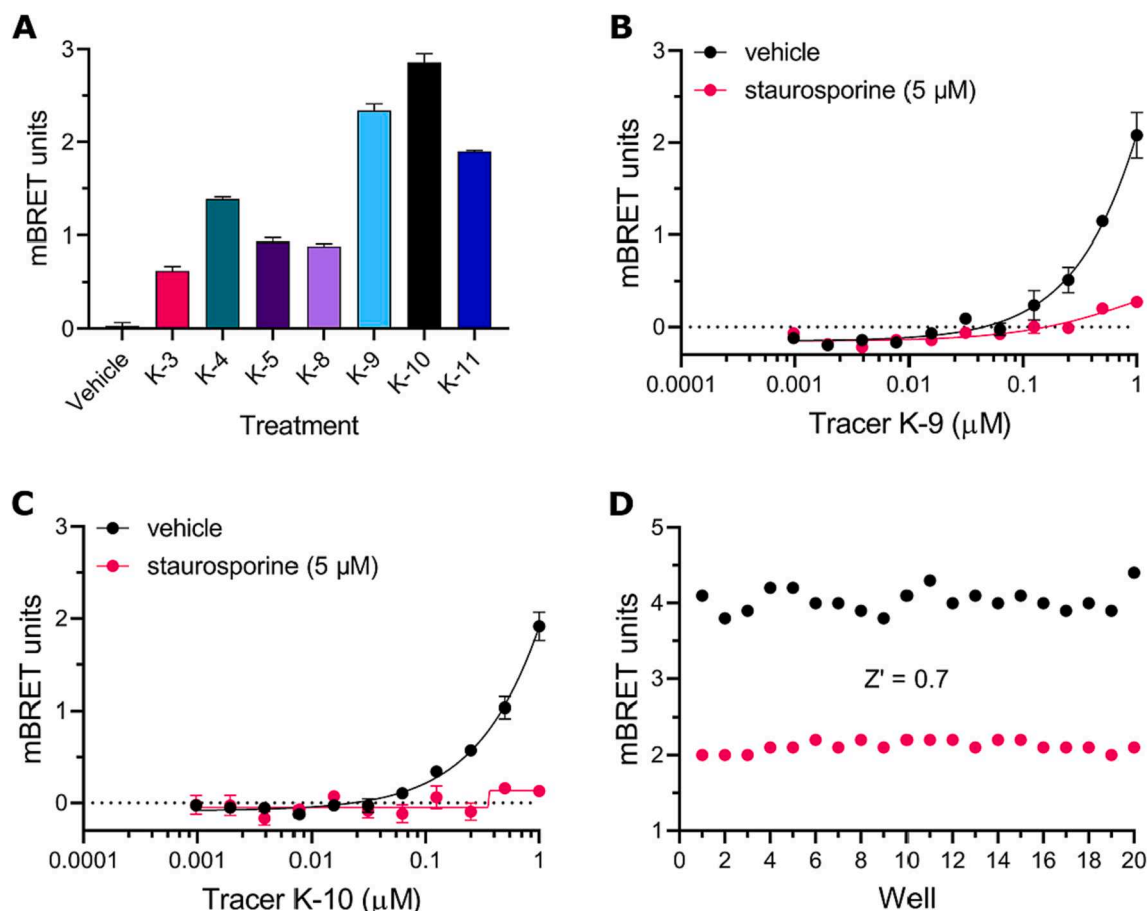


Fig. 2. Development of an in-cell, BRET-based target engagement assay for MKK3. (A) Screening of commercial tracers against MKK3-nLuc expressed in HEK293T cells. The data presented is the mean \pm SEM of a single experiment performed in triplicates. (B) and (C) Titration of Tracer K-9 and K-10 under equilibrium conditions in the presence (pink circles) and absence (black circles) of a saturating concentration of staurosporine (5 μM). The data shown is the mean \pm SEM of a single experiment performed in duplicate. (D) Determination of the Z' -Factor for Tracer K-9 (1 μM). mBRET (mBU) units are calculated as described in the Methods section. (For interpretation of the references to colour in this figure legend, the reader is referred to the web version of this article.)

signal in the presence of seven tracers from Promega's catalog (Fig. 2A). Encouragingly, tracers K-9 and K-10 generated a robust BRET signal, which could be completely displaced by the well-established pan-kinase inhibitor staurosporine (5 μM , Fig. 2B-C). The displacement by staurosporine indicated that the BRET signal was specific to the interaction of the tracer with the ATP binding site of MKK3-Nluc. Furthermore, we estimated this assay to be sensitive and robust, with a Z -factor ≥ 0.5 (Fig. 2D).²¹ Based on these results, we opted to utilize tracer K-9 for subsequent in-cell BRET experiments.

2.3. Discovery of pyrazolo[3,4-*d*]pyrimidines as MKK3 inhibitors

To demonstrate the utility of the tools we developed for MKK3 inhibitor discovery, we applied our TR-FRET MKK3E assay to screen a library comprising approximately 330 bioactive, chemically diverse, and commercially available kinase inhibitors sourced from SelleckChem (Table S1). All compounds were tested at a single concentration of 1 μM (Fig. S3, Table S1). Our results indicated that none of the compounds inhibited MKK3 by more than 65 % at the tested concentration. However, among the screened compounds, the pyrazolo[3,4-*d*]pyrimidine INK128 (Sapanisertinib, **1**) exhibited the highest activity, inhibiting approximately 61 % of MKK3 activity at 1 μM (Fig. 3A).

Compound **1** is a potent ($\text{IC}_{50} < 10 \text{ nM}$) ATP-competitive and cell-permeable inhibitor of mTOR,^{27,28} a phosphoinositide 3-kinase-related protein kinase. Interestingly, within the tested library, three other pyrazolo[3,4-*d*]pyrimidines were capable of inhibiting MKK3 activity by approximately 30 % at 1 μM . PP-242 (Torkinib, **2**) was originally described as a potent ($\text{IC}_{50} < 10 \text{ nM}$) mTOR inhibitor,²⁹ whereas PP1 and PP2 were originally characterized as potent ($\text{IC}_{50} < 10 \text{ nM}$) inhibitors of Src family members.³⁰ The amino acid sequence identity levels between MKK3 and mTOR or Src kinases are quite low ($< 30 \%$), which likely explains the limited MKK3 inhibition potency of these compounds (ranging from 30 % to 61 %) in our assays.

To further confirm the potency of **1** and **2**, we employed our TR-FRET enzymatic assay (Fig. S4). The obtained dose-response curves indicated that inhibitor constants (K_i) values of $1.1 \pm 0.3 \mu\text{M}$ and $1.5 \pm 0.1 \mu\text{M}$, respectively (Fig. 3A). These results indicated that both **1** and **2** are single-digit micromolar inhibitors of MKK3, and suggested compounds having the same pyrazolo[3,4-*d*]pyrimidine scaffold may serve as promising starting points for novel MKK3 inhibitors.

To test these ideas, we acquired and tested three additional pyrazolo[3,4-*d*]pyrimidines originally described as inhibitors of Src protein kinase family members (with IC_{50} values ranging from 3 nM to 1 μM)³¹⁻³³ which were not initially present in our library: 1-NA-PP1 (**3**), 3-BrB-PP1 (**4**), and 1-NM-PP1 (**5**) (Fig. 3B). In our TR-FRET assay, compounds **3-5** were considerably less potent MKK3 inhibitors than **1** and **2**, with K_i values ranging from 4.8 to 27.9 μM . Despite the reduced activity of compounds **3-5**, these results further validated the use of pyrazolo[3,4-

d]pyrimidines as MKK3 inhibitors.

To demonstrate the potential of our set of novel MKK3 tools to support SAR exploration for new MKK3 inhibitors based on the pyrazolo[3,4-*d*]pyrimidine scaffold, we initiated a chemistry program focused on analogues of **2**. This compound was the first ATP-competitive mTOR inhibitor to be described as potent and selective, and is often used in the literature to probe for mTOR inhibition in live cells^{34,35} and animals.^{35,36} Furthermore, structural data detailing the binding mode of **2** to mTOR are available.³⁷

2.4. Design of novel pyrazolo[3,4-*d*]pyrimidine MKK3 inhibitors

To guide our synthetic efforts, we performed molecular dynamic (MD) simulations using a homology model of MKK3 based on MKK7 (PDB ID: 6IB2; 42 % sequence identity) (Fig. 4). We chose to employ a homology model of MKK3 based on MKK7 instead of the available prediction from AlphaFold (ID AF-Q6FHG1-F1)³⁸ due to the latter's representation of the kinase in an inactive conformation, similar to the autoinhibitory conformation found for MKK6 (Fig. S5).^{39,40}

Analysis of trajectories from a 100-ns MD simulation of **2** bound to MKK3 indicated that the compound binding pose was highly stable within the kinase ATP-binding pocket. Notably, the orientation of **2** during the MD simulation exhibited minimal changes when compared to the compound's initial docked pose (Fig. S6). Furthermore, the overall fold of MKK3 was preserved throughout the simulation. The average root mean square deviations (RMSDs) for **2** and the average $\text{C}\alpha$ RMSD values for the entire protein were 0.9 to 4.6 \AA , respectively. These simulations suggested that the indol-hydroxyl group of **2** formed a hydrogen bond with lysine residue K93. This lysine residue is structurally conserved amongst protein kinases and plays a pivotal role in their activity.⁴¹ Additionally, the pyrazolo[3,4-*d*]pyrimidine core of the compound interacted with the protein hinge region via a hydrogen bond to the main chain oxygen of residue E141. These observed interactions between **2** and MKK3 provided insights into the compound's inhibitory activity against the kinase. Furthermore, the N_1 substitution of **2** pointed towards a large cavity at the bottom of MKK3's ATP-binding site, suggesting potential for exploration by bulkier substituents.

Results from our MD simulations encouraged us to generate a set of 19 novel pyrazolo[3,4-*d*]pyrimidine analogs (Table 1). These efforts aimed to expand the chemical space of MKK3 inhibitors by introducing variations in the aromatic substitution at C_3 , including substituted aromatic rings (**8-15**) and heteroaromatic rings (**16-21**). Building upon the MD results, which highlighted the interaction of compound **2** with the critical MKK3 residue K93 through hydrogen bonding, we sought to preserve this interaction. Our approach involved the exploration of different hydrogen bond donor and acceptor moieties at the 3- and 4-positions of the phenyl ring (**22-26**). Scheme 1 depicts the preparation of compounds **8-26**. The process initiated with the utilization of

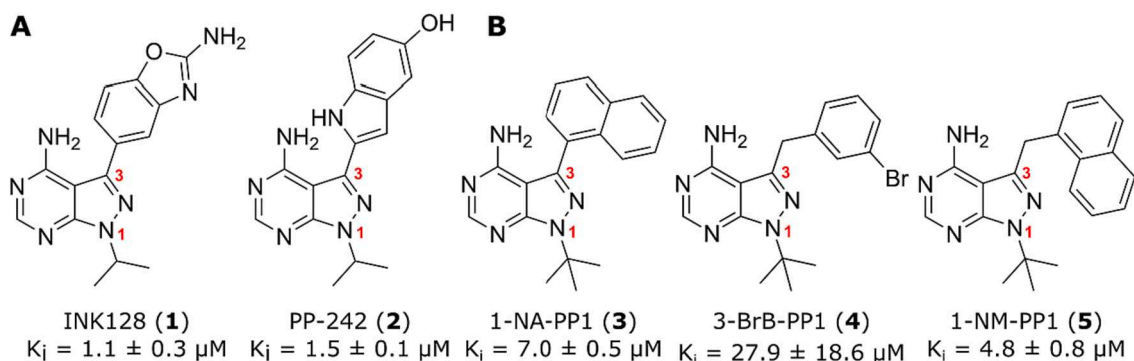


Fig. 3. Structure and inhibition constants (K_i) for selected MKK2 inhibitors. (A) Chemical structure and K_i values of confirmed hits identified from the kinase inhibitor library. (B) Chemical structure and K_i values of related pyrazolo[3,4-*d*]pyrimidines. The data presented represent the mean \pm SEM of two independent experiments, each performed in duplicate.

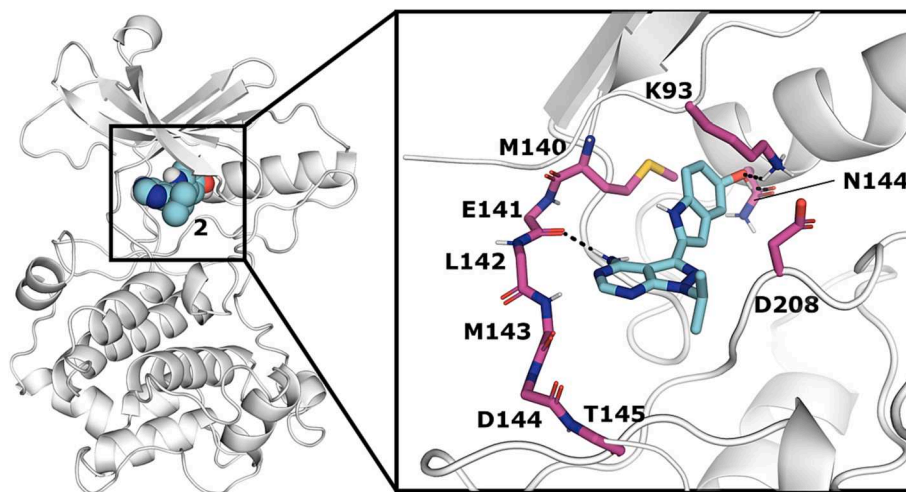


Fig. 4. Overall structure of MKK3 and binding mode to compound **2** following a 100-ns MD Simulation. The protein is depicted as a white cartoon, while the atoms of **2** are represented as spheres and sticks, with carbon atoms colored cyan. The inset provides details of the binding interaction of **2** with MKK3. The kinase hinge region (residues 140–145), the structurally-conserved and catalytically important lysine (K93) and aspartic acid (D208), and asparagine 144 are depicted as colored sticks (carbon atoms in magenta), with parts of the protein cartoon representation omitted for clarity. Dashed black lines indicate potential hydrogen bonds between MKK3 and **2**. (For interpretation of the references to colour in this figure legend, the reader is referred to the web version of this article.)

commercially available 4-chloro-pyrazolo[3,4-*d*]pyrimidine **7**, which underwent nucleophilic displacement with NH_4OH , followed by bromine installation at C_3 . Subsequent Suzuki coupling using various boronic acids led to the generation of the desired target compounds **8–26**.

2.5. Activity of novel pyrazolo[3,4-*d*]pyrimidine compounds against MKK3E

This set of pyrazolo[3,4-*d*]pyrimidine compounds was initially evaluated against MKK3E at a single concentration of $5\ \mu\text{M}$ using our TR-FRET assay. For the most potent compounds (>30 % inhibition), we determined K_i values from complete dose–response curves (Table 1; Fig. S7).

Compound **8**, which has an unsubstituted benzyl group at position C_3 , inhibited MKK3E with a K_i of $9.3 \pm 0.8\ \mu\text{M}$, further confirming the inhibitory properties of the pyrazolo[3,4-*d*]pyrimidine core. Attempts to improve the potency of **8** by introducing heteroatoms at various positions on the benzene ring at C_3 (**9–15**) did not yield the desired improvements. Nonetheless, these studies indicated that addition of a 2-Cl (**9**, $K_i = 11.0 \pm 0.9\ \mu\text{M}$) or 3-F (**12**; $K_i = 15.0 \pm 7.7\ \mu\text{M}$) were tolerated by the enzyme. However, once both heteroatoms were added to the benzene ring as in compound **10** (2-Cl, 3-F), the activity dropped significantly ($K_i = 27.5 \pm 6.7\ \mu\text{M}$). Besides, by changing the positions to 3-Cl, 4-F the activity improved approximately 3-fold for compound **11** ($K_i = 9.9 \pm 1.4\ \mu\text{M}$) as an indication that MKK3 might accommodate larger substituents in these positions without affecting compound activity.

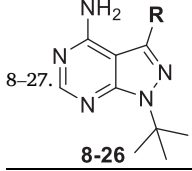
Next, we explored the use of compounds with fused heteroaromatic rings as substituents at C_3 (**16–21**). These modifications were inspired by **1–5**, which have bulkier and polar substituents at this position and were shown to be more active than **9–15**. Enzyme inhibition data for the quinolines **16–17**, the isoquinoline **18** and the naphthylamine **19** suggested that bulkier groups at C_3 increased compound potency compared to **8**. However, the extent of this potency enhancement depended on the specific position of the nitrogen-containing group. For instance, compounds **16** (quinoline with *N* at position 5, $K_i = 6.2 \pm 0.7\ \mu\text{M}$) and **19** (4-naphthylamine, $K_i = 7.1 \pm 0.9\ \mu\text{M}$) had similar potencies against MKK3E activity and possessed nitrogen atoms that potentially occupy equivalent positions within the enzyme's ATP-binding site. Conversely, compounds **17** and **18**, with *N* atoms in disparate positions, failed to

inhibit MKK3. These findings were corroborated by the results obtained with naphthylamine **20** ($K_i = 6.5 \pm 2.1\ \mu\text{M}$), which featured an *N* potentially occupying the same position within MKK3's ATP-binding site of those in **16** and **20**, and the lack of activity of indazole **21**, having the *N* atom in a disparate position. Interestingly, our results also underscored the significance of the nitrogen's atom position over its protonation state.

Overall, these observations were consistent with the results from MD simulations, indicating that polar substitutions at C_3 could interact with a polar region within the enzyme's ATP-binding site, primarily composed of hydrophilic residues. This region included two structurally conserved and catalytically-important residues (K93 and D208) and N144. Consequently, we decided to explore additional polar substitutions at the aromatic ring using compounds **22–27**. Unfortunately, the installation of *N*-substituted amides (**22**, **24** and **25**) or sulfonamide (**23**) at *meta*- or *para*- positions was deleterious to the activity. The bulkier size of these substituents may interfere with MKK3 binding leading to the compounds lack of activity. On the other hand, a smaller 3,5-difluorophenol substitution (**26**) that mimics the phenol substituent in **2** was well tolerated, indicating that polarity and size at the C_3 position are important for MKK3 binding. The 3,5-difluorophenol substitution was chosen due to the enhanced acidity of the phenol flanked by two fluorine atoms, that act as electron-withdrawing groups. This moiety has been extensively studied by medicinal chemists in kinase drug discovery^{42,43} because the phenol oxygen often interacts with the basic catalytic lysine in the back of the ATP pocket.^{44,45} To test this hypothesis, we conducted 100-ns MD simulations of **26** bound to MKK3. The results revealed a stable interaction via hydrogen bonding of the phenol oxygen with K93 and D208 (Fig.S8). Moreover, the pyrazolo[3,4-*d*]pyrimidine maintains the hydrogen bond with the backbone of E141 in the hinge, as observed by other authors.^{32,46,47}

Analysis of Ligand Efficiency (LE) is defined as an approach for scaling compound affinity differences by the corresponding molecular size differences. This strategy is particularly helpful in SAR analysis for compound optimization and prioritization.^{48–50} Lipophilicity is another important parameter in drug discovery and is often used to prioritize hit compounds. The lipophilicity-corrected ligand efficiency (LELP) is defined as the ratio of the logarithm of the calculated *n*-octanol–water partition coefficient (clog*P*) and LE.⁵¹ There is no consensus in the literature on the optimal values for a lead compound or drug candidate, however, historically, the range of values for LE and LELP for lead

Table 1
Inhibition potency and ligand efficiency properties of compounds



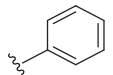
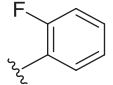
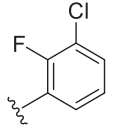
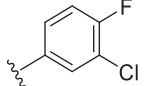
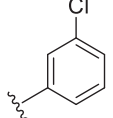
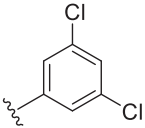
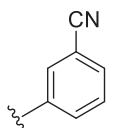
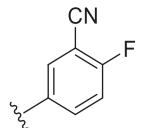
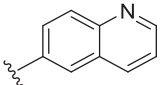
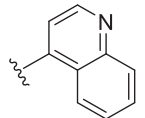
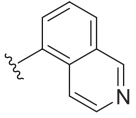
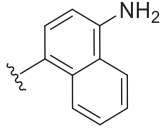
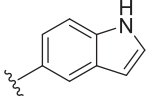
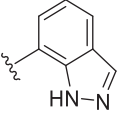
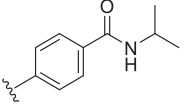
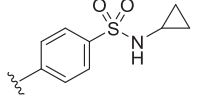
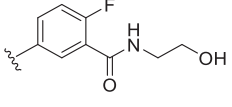
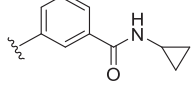
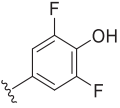
Entry	R	Inhibition (%) ^a	K _i (μM) ^b	LE ^c	LLEP ^d
8		34.8 ± 5.5	9.3 ± 0.8	0.4	9
9		37.4 ± 0.3	11.0 ± 0.9	0.3	10
10		35.2 ± 1.6	27.5 ± 6.7	0.3	13
11		39.3 ± 0.1	9.9 ± 1.4	0.3	12
12		19.8 ± 3.3	15.0 ± 7.7	0.3	11
13		23.4 ± 0.8	n.d.	n.d.	n.d.
14		Not active ^e	n.d.	n.d.	n.d.
15		3.4 ± 12.9	n.d.	n.d.	n.d.
16		35.6 ± 9.6	6.2 ± 0.7	0.3	11
17		28.2 ± 3.3	n.d.	n.d.	n.d.

Table 1 (continued)

Entry	R	Inhibition (%) ^a	K _i (μM) ^b	LE ^c	LLEP ^d
18		12.4 ± 5.8	n.d.	n.d.	n.d.
19		54.8 ± 1.2	7.1 ± 0.9	0.3	11
20		58.2 ± 6.4	6.5 ± 2.1	0.3	8
21		Not active ^e	n.d.	n.d.	n.d.
22		26.4 ± 0.2	n.d.	n.d.	n.d.
23		12.6 ± 1.3	n.d.	n.d.	n.d.
24		5.2 ± 3.8	n.d.	n.d.	n.d.
25		7.1 ± 1.9	n.d.	n.d.	n.d.
26		44.9 ± 2.2	4.6 ± 0.6	0.3	9

n.d. = not determined.

^a Data shown is mean ± SEM (n = 2/compound) of a single experiment.

^b Data shown are mean ± SEM (n = 2/concentration) of two independent experiments.

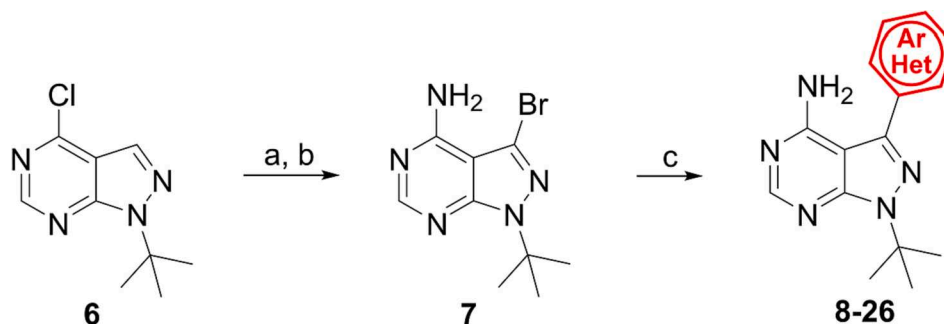
^c LE: ligand efficiency = (1.37 × pK_i)/HAC, where pK_i = -log(K_i) in the molar range; HAC = heavy atom count.

^d LLEP: lipophilic ligand efficiency = clogP/LE, where clogP = calculated partition coefficient, calculated with ChemDraw v.22.0.0.22.

^e Not active – inhibitory activity lower than the expected assay limit.

compounds has been reported as 0.3–0.5 and 7–10, respectively.^{52,53}

In agreement with our previous observation, compound **26** displayed the best inhibitory activity from the series of compounds tested, with a K_i of 4.6 ± 0.6 μM and a favorable ligand efficiency (LE = 0.3; LLEP = 9), therefore **26** was selected for further validation in the BRET assay.



Scheme 1. Reagents and conditions: (a) 1,4-dioxane, NH_4OH , r.t., to 100°C , 18 h, 89 %; (b) Br_2 , H_2O , r.t. 1 h, then 100°C , 45 min, 94 %; (c) $\text{Pd}(\text{dppf})\text{Cl}_2$, 1,4-dioxane, **7**, Cs_2CO_3 , boronic acid, N_2 , 100°C , 18 h, 7–91 %.

2.6. Compound 26 binds to MKK3 in human cells

To assess compound **2** and **26** ability to bind to MKK3 in intact human cells, we used the BRET-based in-cell target engagement assay as described previously. Our results indicated that **2** failed to fully displace the tracer at concentrations of up to $100\ \mu\text{M}$ (Fig. 5A). This limitation was consistent with prior reports noting the low aqueous solubility of **2** (6–9 $\mu\text{g}/\text{mL}$ in water).^{36,54} In contrast, we were able to use significantly higher concentrations of **26** in our assay, reaching up to 1 mM. This extended concentration range enabled the generation of a complete dose–response curve, from which we calculated a cellular IC_{50} of $144.7 \pm 10.2\ \mu\text{M}$ (Fig. 5B). These results demonstrate a significant disparity between the *in vitro* and cellular efficacies of compound **26**. This discrepancy could be attributed to a multitude of factors. One possibility is the compound's limited cell permeability, which might impede its access to intracellular targets. Additionally, the compound's efficacy might be adversely affected by the ATP-rich intracellular environment, where it faces competition with ATP for binding to the kinase. Moreover, metabolic instability or active efflux mechanisms within the cells could also contribute to the reduced cellular activity. Future investigations will be dedicated to enhancing the in-cell activity of compound **26**,

potentially through modifications aimed at improving cell permeability and metabolic stability.

2.7. Selectivity profile of compounds 2 and 26

The human genome encodes more than 500 proteins having a structurally conserved kinase domain.⁵⁵ The majority of kinase inhibitors bind to the ATP-binding pocket, a structurally conserved region within the kinase domain. To assess the ability of compounds **2** and **26** to bind to 28 different human protein kinases, we used a TR-FRET assay based on the competitive displacement of a generic, ATP competitive fluorescent ligand.

This kinase panel, albeit limited, included representatives from all protein kinase superfamilies. (Fig. S9). Our results indicated that, in these assays, **26** was able to displace more than 80 % of the fluorescent tracer from two out of the 28 tested human protein kinases (DAPK3 and RIPK2). In contrast, **2** had a similar tracer displacement level for six of these kinases (DMPK1, DAPK3, RIPK2, SLK, DYRK2, and TGF β R2) (Fig. 5C, Table S2).

Among the human kinases within our panel, **2** was previously shown to strongly inhibit DYRK2 and PKAC α activity *in vitro*.⁵⁶ Nevertheless, in

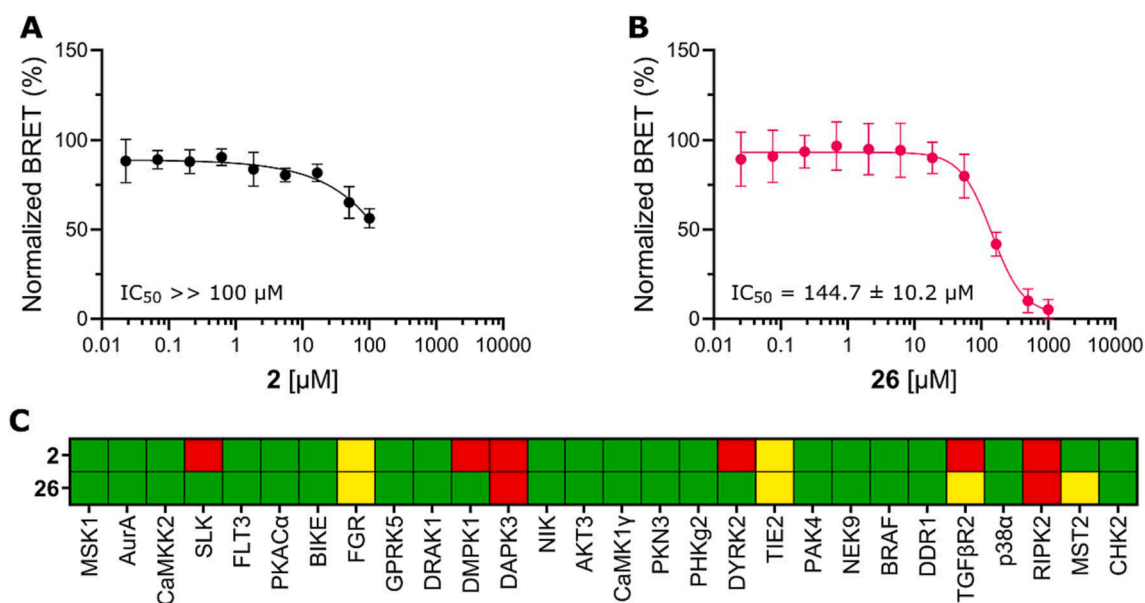


Fig. 5. In-cell target engagement and selectivity profiles of compounds **2** and **26**. (A, B) Representative curves illustrating competitive displacement experiments of K-9 (1.0 μM) by compounds **2** (A) and **26** (B) in human cells. Data presented are the mean \pm SD ($n = 3$ per concentration) of two independent experiments. (C) Selectivity profiles of compounds **2** and **26**. The compounds were subjected to a tracer displacement assay at a single concentration (1 μM) against a panel of 28 human kinases. The ability of compounds to displace the tracer compared to the vehicle control is depicted by colored squares: red (>80 % displacement), yellow (40–80 % displacement), and green (<40 % displacement). (For interpretation of the references to colour in this figure legend, the reader is referred to the web version of this article.)

our tracer-displacement assay, we did not observe robust binding between **2** and PKA α . These discrepancies may be attributed to the differences in assay formats employed (enzyme activity versus tracer displacement), necessitating further investigations to clarify these discrepancies.

3. Conclusions

In summary, our study has addressed critical challenges in the development of MKK3 inhibitors, a relatively understudied kinase that lacks tool compounds for deciphering its role in both disease and normal biology. Therefore, we aimed to develop new methodologies for screening compounds against this kinase *in vitro* and *in cellulo*. We demonstrated the validity of our assays by screening commercial kinase inhibitors, resulting in the generation of a novel pyrazolo[3,4-*d*]pyrimidine, compound **26**, with improved activity against MKK3, especially in the context of live cells, and fewer off-target effects than its parent compound **2**. We believe these assays will pave the way for a new generation of MKK3 inhibitors with optimized potency and selectivity, enabling researchers to uncover the specific roles of MKK3 in cell biology.

4. Experimental procedures

4.1. Chemistry

The final compounds were characterized by $^1\text{H}/^{13}\text{C}$ NMR and electrospray ionization-mass spectrometry (ESI-MS). NMR spectra were recorded on a Bruker 250 MHz, 400 MHz, or 500 MHz spectrometers. ^1H and proton decoupled ^{13}C NMR spectra were scanned on a Bruker Avance NMR spectrometer in DMSO- d_6 , CDCl_3 , Methanol- d_4 or Acetone- d_6 at 250 MHz (^1H), 400 MHz (^1H) and 101 MHz (^{13}C) or 500 MHz (^1H) and 126 MHz (^{13}C). The chemical shifts (δ) are reported in ppm. Sample was submitted for MS analysis to control the exact mass of the compound synthesized. Compounds containing chlorine or bromine were measured by their most abundant isotope (^{34}Cl and ^{79}Br , respectively). 1 μL of the sample (diluted for a final concentration of 0.1 $\mu\text{g}/\mu\text{L}$ in 100 % acetonitrile) was analyzed by reverse phase HPLC-ESI-MS using an Acquity H-class HPLC system (Waters Corp. Milford, MA, USA) which is directly connected to the XEVO G2 Sx Q-ToF (Waters) to determine the intact mass of the small molecule. The HPLC is equipped with C18 column (ACQUITY UPLC Protein BEH C18 Column, 1.7 μm , 2.1 mm X 50 mm, Waters) for small molecule separation kept at 45 $^\circ\text{C}$. The mobile phase solvent A was 0.1 % Formic acid (FA) in water, and solvent B was 0.1 % FA in 100 % Acetonitrile (ACN). The samples were loaded at a flow rate of 0.5 $\mu\text{L}/\text{min}$, and eluted from C18 column at a flow rate of 400 $\mu\text{L}/\text{min}$ with one linear gradient step: one from 3 to 90 % solvent B over 2.5 min. The column was regenerated by washing at 100 % solvent B for 1.5 min and re-equilibrated at 1 % solvent B for 3 min. Exact mass analysis was performed in positive ion electrospray in resolution mode. For internal calibration, the lockspray properties were the following: scan time was fixed at 0.5 s, with a mass window of 0.5 Da around Leu-enkephalin (556.2771 Da). The ToF-MS acquisition ranged from 50 Da to 2,000 Da with a scan time fixed at 0.5 s. The cone voltage on the ESI source was fixed at 40 V. MS Raw data was analyzed using MassLynx software developed by Waters. All reagents were purchased from commercial source and used as received.

4.1.1. 3-bromo-1-(tert-butyl)-1H-pyrazolo[3,4-*d*]pyrimidin-4-amine **7**

To a stirred solution of 4-chloro-pyrazolo[3,4-*d*]pyrimidine (**6**, 1.46 mmol) in 1,4-dioxane (5 mL) was added NH_4OH (10 mL) at room temperature. The reaction mixture was heated at 100 $^\circ\text{C}$ overnight. The reaction mixture was cooled, and the solvents were removed under reduced pressure. The solids formed were collected as a white solid in 89 % yield, with enough purity. A mixture the previously obtained compound and bromine in water was stirred at room temperature for 1

h. and at 100 $^\circ\text{C}$ for 30 min. To increase the solubilizing power of the reaction mixture, ethyl acetate was added, and the resulting solution was heated at reflux for an additional 15 min. The two layers were separated, and the aqueous phase was extracted with ethyl acetate. The combined organic extracts were washed with 5 % aqueous NaHSO_3 solution, followed by brine and the organic solvent was dried (MgSO_4) and concentrated under reduced pressure. The resulting material was passed through a pad of silica and was dried to afford **7** a yellow solid in 94 % yield (123 mg). ^1H NMR (500 MHz, CDCl_3) δ 8.23 (s, 1H), 1.78 (s, 9H). Compound **7** (CAS no: 862728–61-8) ^1H NMR was in accordance with previous publications.^{57–59}

4.1.2. General procedure for the synthesis of **8–27**

To a solution of $\text{Pd}(\text{dppf})\text{Cl}_2$ (10 mol%) in degassed 1,4-dioxane (1 mL) was added **7** (50 mg, 0.186 mmol), Cs_2CO_3 (152 mg, 0.465 mmol) and boronic acid (0.223 mmol). The flask was sealed under N_2 and the reaction mixture was stirred at 100 $^\circ\text{C}$ for overnight, filtered through Celite and concentrated under reduced pressure. The residue was purified by column chromatography.

4.1.3. 1-(tert-butyl)-3-phenyl-1H-pyrazolo[3,4-*d*]pyrimidin-4-amine **8**

The product **8** was obtained as a pale white solid in 60 % yield (30 mg). ^1H NMR (400 MHz, CDCl_3) δ 8.38 (s, 1H), 7.72 (d, $J = 7.8$ Hz, 2H), 7.55 (t, $J = 7.5$ Hz, 2H), 7.48 (t, $J = 7.3$ Hz, 1H), 5.51 (s, 2H), 1.86 (s, 9H). ^{13}C NMR (126 MHz, CDCl_3) δ 157.8, 154.4, 154.2, 142.1, 133.8, 129.3, 128.8, 128.6, 99.7, 60.5, 29.2. HR-MS m/z calculated for $\text{C}_{15}\text{H}_{18}\text{N}_5$: 268.1557 [M + H] $^+$, found 268.1560 [M + H] $^+$.

4.1.4. 1-(tert-butyl)-3-(2-fluorophenyl)-1H-pyrazolo[3,4-*d*]pyrimidin-4-amine **9**

The product **9** was obtained as a pale yellow solid in 64 % yield (34 mg). ^1H NMR (500 MHz, DMSO) δ 8.23 (s, 1H), 7.55 (dd, $J = 13.5$, 7.2 Hz, 2H), 7.40–7.32 (m, 2H), 1.74 (s, 9H). ^{13}C NMR (126 MHz, DMSO) δ 161.0, 159.0, 158.6, 155.2, 154.0, 136.2, 132.2, 131.6, 131.5, 125.4, 125.4, 121.4, 121.3, 116.9, 116.8, 100.5, 60.3, 29.2. HR-MS m/z calculated for $\text{C}_{15}\text{H}_{17}\text{FN}_5$: 286.1463 [M + H] $^+$, found 286.1489 [M + H] $^+$.

4.1.5. 1-(tert-butyl)-3-(3-chloro-2-fluorophenyl)-1H-pyrazolo[3,4-*d*]pyrimidin-4-amine **10**

The product **10** was obtained as a pale yellow solid in 54 % yield (32 mg). ^1H NMR (500 MHz, DMSO) δ 8.23 (s, 1H), 7.71–7.66 (m, 1H), 7.52–7.47 (m, 1H), 7.34 (t, $J = 7.9$ Hz, 1H), 1.74 (s, 9H). ^{13}C NMR (126 MHz, DMSO) δ 158.5, 156.8, 155.3, 154.6, 154.1, 135.4, 131.6, 131.0, 126.1, 126.0, 123.2, 123.1, 121.3, 121.2, 100.4, 60.4, 29.2. HR-MS m/z calculated for $\text{C}_{15}\text{H}_{16}\text{ClFN}_5$: 320.1073 [M + H] $^+$, found 320.1086 [M + H] $^+$.

4.1.6. 1-(tert-butyl)-3-(3-chloro-4-fluorophenyl)-1H-pyrazolo[3,4-*d*]pyrimidin-4-amine **11**

The product **11** was obtained as a pale yellow solid in 79 % yield (47 mg). ^1H NMR (500 MHz, DMSO) δ 8.25 (s, 1H), 7.78 (dd, $J = 7.2$, 1.9 Hz, 1H), 7.65–7.60 (m, 1H), 7.56 (t, $J = 8.9$ Hz, 1H), 1.75 (s, 9H). ^{13}C NMR (126 MHz, DMSO) δ 158.8, 158.7, 156.9, 155.2, 154.5, 140.1, 131.4, 131.4, 130.9, 129.6, 129.6, 120.6, 120.4, 118.0, 117.8, 99.1, 60.3, 29.2. HR-MS m/z calculated for $\text{C}_{15}\text{H}_{16}\text{ClFN}_5$: 320.1073 [M + H] $^+$, found 320.1086 [M + H] $^+$.

4.1.7. 1-(tert-butyl)-3-(3-chlorophenyl)-1H-pyrazolo[3,4-*d*]pyrimidin-4-amine **12**

The product **12** was obtained as a yellow solid in 67 % yield (37 mg). ^1H NMR (250 MHz, DMSO) δ 8.26 (s, 1H), 7.67 (s, 1H), 7.65–7.49 (m, 3H), 6.87 (s, 2H), 1.76 (s, 9H). ^{13}C NMR (126 MHz, DMSO) δ 158.3, 154.7, 154.0, 140.3, 135.3, 133.6, 130.9, 128.3, 128.0, 127.0, 98.7, 59.9, 28.7. HR-MS m/z calculated for $\text{C}_{15}\text{H}_{17}\text{ClN}_5$: 302.1167 [M + H] $^+$, found 302.1166 [M + H] $^+$.

4.1.8. 1-(*tert*-butyl)-3-(3,5-dichlorophenyl)-1*H*-pyrazolo[3,4-*d*]pyrimidin-4-amine **13**

The product **13** was obtained as a pale yellow solid in 7 % yield (4.4 mg). ^1H NMR (500 MHz, DMSO) δ 8.26 (s, 1H), 7.69 (t, $J = 1.9$ Hz, 1H), 7.63 (d, $J = 1.9$ Hz, 2H), 1.76 (s, 9H). ^{13}C NMR (126 MHz, DMSO) δ 158.73, 155.2, 154.6, 139.6, 136.9, 134.9, 128.2, 127.5, 99.2, 60.5, 29.1. HR-MS m/z calculated for $\text{C}_{15}\text{H}_{16}\text{Cl}_2\text{N}_5$: 336.0777 [M + H] $^+$, found 336.0801 [M + H] $^+$.

4.1.9. 3-(4-amino-1-(*tert*-butyl)-1*H*-pyrazolo[3,4-*d*]pyrimidin-3-yl)benzonitrile **14**

The product **14** was obtained as a yellow solid in 39 % yield (21 mg). ^1H NMR (250 MHz, DMSO) δ 8.26 (s, 1H), 8.03 (s, 1H), 8.01 – 7.88 (m, 2H), 7.72 (t, $J = 7.8$ Hz, 1H), 6.97 (s, 2H), 1.76 (s, 9H). ^{13}C NMR (126 MHz, DMSO) δ 158.3, 154.8, 154.2, 139.8, 134.4, 133.00, 131.9, 131.8, 130.2, 118.8, 112.2, 98.7, 60.0, 28.7. HR-MS m/z calculated for $\text{C}_{16}\text{H}_{17}\text{N}_6$: 293.1509 [M + H] $^+$, found 293.1528 [M + H] $^+$.

4.1.10. 5-(4-amino-1-(*tert*-butyl)-1*H*-pyrazolo[3,4-*d*]pyrimidin-3-yl)-2-fluorobenzonitrile **15**

The product **15** was obtained as a yellow solid in 44 % yield (25 mg). ^1H NMR (250 MHz, DMSO) δ 8.26 (s, 1H), 8.09 (dd, $J = 6.2, 2.2$ Hz, 1H), 8.00 (ddd, $J = 8.6, 5.3, 2.3$ Hz, 1H), 7.66 (t, $J = 9.1$ Hz, 1H), 7.01 (s, 2H), 1.75 (s, 9H). ^{13}C NMR (126 MHz, DMSO) δ 163.5, 161.5, 158.2, 154.8, 154.1, 139.1, 136.0, 135.9, 133.7, 130.7, 130.769, 117.2, 117.1, 114.0, 101.0, 100.9, 98.8, 59.9, 28.7. HR-MS m/z calculated for $\text{C}_{16}\text{H}_{16}\text{FN}_6$: 311.1415 [M + H] $^+$, found 311.1432 [M + H] $^+$.

4.1.11. 1-(*tert*-butyl)-3-(quinolin-4-yl)-1*H*-pyrazolo[3,4-*d*]pyrimidin-4-amine **16**

The product **16** was obtained as a pale yellow solid in 82 % yield (48 mg). ^1H NMR (400 MHz, DMSO) δ 9.00 (d, $J = 4.4$ Hz, 1H), 8.29 (s, 1H), 8.13 (d, $J = 8.1$ Hz, 1H), 8.05 (dd, $J = 8.4, 0.7$ Hz, 1H), 7.81 (ddd, $J = 8.3, 6.9, 1.3$ Hz, 1H), 7.63 (ddd, $J = 8.2, 6.9, 1.2$ Hz, 1H), 7.58 (d, $J = 4.4$ Hz, 1H), 1.79 (s, 9H). ^{13}C NMR (126 MHz, DMSO) δ 158.4, 155.4, 154.2, 150.8, 148.9, 138.8, 138.3, 130.0, 129.9, 127.6, 126.8, 126.5, 123.1, 100.6, 60.6, 29.2. HR-MS m/z calculated for $\text{C}_{18}\text{H}_{19}\text{N}_6$: 319.1666 [M + H] $^+$, found 319.1683 [M + H] $^+$.

4.1.12. 1-(*tert*-butyl)-3-(quinolin-5-yl)-1*H*-pyrazolo[3,4-*d*]pyrimidin-4-amine **17**

The product **17** was obtained as a pale yellow solid in 82 % yield (48 mg). ^1H NMR (400 MHz, CDCl_3) δ 9.01 (dd, $J = 4.1, 1.6$ Hz, 1H), 8.43 (s, 1H), 8.40 (d, $J = 8.5$ Hz, 1H), 8.27 (d, $J = 8.5$ Hz, 1H), 7.91 – 7.84 (m, 1H), 7.77 (dd, $J = 7.1, 1.0$ Hz, 1H), 7.47 (dd, $J = 8.6, 4.2$ Hz, 1H), 5.12 (s, 2H), 1.91 (s, 9H). ^{13}C NMR (126 MHz, CDCl_3) δ 157.6, 154.7, 154.1, 151.0, 148.7, 139.2, 134.5, 131.0, 129.0, 128.5, 127.2, 122.0, 60.8, 29.3. HR-MS m/z calculated for $\text{C}_{18}\text{H}_{19}\text{N}_6$: 319.1666 [M + H] $^+$, found 319.1683 [M + H] $^+$.

4.1.13. 1-(*tert*-butyl)-3-(isoquinolin-5-yl)-1*H*-pyrazolo[3,4-*d*]pyrimidin-4-amine **18**

The product **18** was obtained as a pale yellow solid in 69 % yield (41 mg). ^1H NMR (500 MHz, DMSO) δ 9.43 (s, 1H), 8.53 (d, $J = 5.9$ Hz, 1H), 8.29 (s, 1H), 8.27 (d, $J = 8.2$ Hz, 1H), 7.89 (dd, $J = 7.1, 1.1$ Hz, 1H), 7.83 (d, $J = 8.0$ Hz, 1H), 7.81 – 7.78 (m, 1H), 1.80 (s, 9H). ^{13}C NMR (126 MHz, DMSO) δ 158.5, 155.3, 154.1, 153.3, 144.1, 139.3, 134.4, 132.9, 129.8, 129.3, 129.1, 127.7, 118.8, 100.7, 60.4, 29.3. HR-MS m/z calculated for $\text{C}_{18}\text{H}_{19}\text{N}_6$: 319.1666 [M + H] $^+$, found 319.1683 [M + H] $^+$.

4.1.14. 3-(4-aminonaphthalen-1-yl)-1-(*tert*-butyl)-1*H*-pyrazolo[3,4-*d*]pyrimidin-4-amine **19**

The product **19** was obtained as a pale yellow solid in 55 % yield (34 mg). ^1H NMR (500 MHz, DMSO) δ 8.24 (s, 1H), 8.20 (dd, $J = 6.5, 3.2$ Hz, 1H), 7.72 (dd, $J = 6.5, 3.2$ Hz, 1H), 7.44 (dd, $J = 6.5, 3.3$ Hz, 2H), 7.33

(d, $J = 7.7$ Hz, 1H), 6.80 (d, $J = 7.7$ Hz, 1H), 6.10 (s, 2H), 1.78 (s, 9H). ^{13}C NMR (126 MHz, DMSO) δ 158.5, 155.2, 153.8, 146.5, 141.5, 132.9, 129.9, 127.0, 125.8, 124.5, 123.3, 123.1, 117.3, 107.3, 101.1, 59.9, 29.4. HR-MS m/z calculated for $\text{C}_{19}\text{H}_{19}\text{N}_6$: 333.1822 [M + H] $^+$, found 333.1826 [M + H] $^+$.

4.1.15. 1-(*tert*-butyl)-3-(1*H*-indol-5-yl)-1*H*-pyrazolo[3,4-*d*]pyrimidin-4-amine **20**

The product **20** was obtained as a pale white solid in 26 % yield (15 mg). ^1H NMR (400 MHz, CDCl_3) δ 8.42 (s, 1H), 8.38 (s, 1H), 7.96 (s, 1H), 7.58 – 7.49 (m, 2H), 7.33 (t, $J = 2.6$ Hz, 1H), 6.66 (s, 1H), 5.51 (s, 2H), 1.88 (s, 9H). ^{13}C NMR (126 MHz, CDCl_3) δ 157.9, 154.3, 154.1, 143.5, 136.0, 128.5, 125.4, 125.3, 122.7, 121.2, 111.9, 103.2, 99.9, 60.3, 29.3. HR-MS m/z calculated for $\text{C}_{17}\text{H}_{19}\text{N}_6$: 307.1666 [M + H] $^+$, found 307.1708 [M + H] $^+$.

4.1.16. 1-(*tert*-butyl)-3-(1*H*-indazol-7-yl)-1*H*-pyrazolo[3,4-*d*]pyrimidin-4-amine **21**

The product **21** was obtained as a pale yellow solid in 38 % yield (22 mg). ^1H NMR (500 MHz, DMSO) δ 12.99 (s, 1H), 8.29 (s, 1H), 8.21 (s, 1H), 7.88 (d, $J = 8.0$ Hz, 1H), 7.51 (d, $J = 7.0$ Hz, 1H), 7.32 – 7.25 (m, 1H), 1.82 (s, 9H). ^{13}C NMR (126 MHz, DMSO) δ 158.7, 155.1, 154.1, 138.7, 138.5, 134.4, 126.7, 124.3, 121.4, 121.3, 116.8, 99.8, 60.4, 29.0. HR-MS m/z calculated for $\text{C}_{16}\text{H}_{18}\text{N}_7$: 308.1618 [M + H] $^+$, found 308.1651 [M + H] $^+$.

4.1.17. 4-(4-amino-1-(*tert*-butyl)-1*H*-pyrazolo[3,4-*d*]pyrimidin-3-yl)-*N*-isopropylbenzamide **22**

The product **22** was obtained as a yellow solid in 60 % yield (39 mg). ^1H NMR (250 MHz, DMSO) δ 8.33 (d, $J = 7.8$ Hz, 1H), 8.26 (s, 1H), 8.02 (d, $J = 8.3$ Hz, 2H), 7.73 (d, $J = 8.3$ Hz, 2H), 6.80 (bs, 2H), 4.15 (dq, $J = 13.3, 6.6$ Hz, 1H), 1.77 (s, 9H), 1.20 (d, $J = 6.6$ Hz, 6H). ^{13}C NMR (126 MHz, DMSO) δ 164.9, 158.3, 154.7, 154.0, 141.0, 135.6, 134.4, 128.1, 128.0, 98.8, 59.8, 41.1, 28.7, 22.4. HR-MS m/z calculated for $\text{C}_{19}\text{H}_{25}\text{N}_6\text{O}$: 353.2084 [M + H] $^+$, found 353.2091 [M + H] $^+$.

4.1.18. 4-(4-amino-1-(*tert*-butyl)-1*H*-pyrazolo[3,4-*d*]pyrimidin-3-yl)-*N*-cyclopropylbenzenesulfonamide **23**

The product **23** was obtained as a white solid in 15 % yield (11 mg). ^1H NMR (500 MHz, CDCl_3) δ 8.39 (s, 1H), 8.09 (d, $J = 8.1$ Hz, 2H), 7.91 (d, $J = 8.1$ Hz, 2H), 5.60 (s, 2H), 5.53 (s, 1H), 2.37 – 2.30 (m, 1H), 1.86 (s, 9H), 0.75 – 0.64 (m, 4H). ^{13}C NMR (126 MHz, CDCl_3) δ 157.6, 154.5, 154.4, 140.3, 139.9, 138.2, 129.1, 128.3, 99.7, 61.0, 29.2, 24.3, 6.3. HR-MS m/z calculated for $\text{C}_{18}\text{H}_{23}\text{N}_6\text{O}_2\text{S}$: 387.1598 [M + H] $^+$, found 387.1603 [M + H] $^+$.

4.1.19. 5-(4-amino-1-(*tert*-butyl)-1*H*-pyrazolo[3,4-*d*]pyrimidin-3-yl)-2-fluoro-*N*-(2-hydroxyethyl)benzamide **24**

The product **24** was obtained as a pale yellow solid in 91 % yield (63 mg). ^1H NMR (500 MHz, DMSO) δ 8.31 (d, $J = 2.2$ Hz, 1H), 8.25 (s, 1H), 7.87 (dd, $J = 6.9, 2.3$ Hz, 1H), 7.77 (ddd, $J = 8.2, 4.8, 2.3$ Hz, 1H), 7.44 (dd, $J = 10.3, 8.6$ Hz, 1H), 4.76 (t, $J = 5.5$ Hz, 1H), 3.53 (q, $J = 6.0$ Hz, 2H), 3.39 – 3.35 (m, 2H), 1.76 (s, 9H). ^{13}C NMR (126 MHz, DMSO) δ 163.9, 160.7, 158.7, 155.2, 154.4, 140.7, 132.6, 132.6, 130.4, 130.0, 125.0, 124.8, 117.5, 117.3, 99.1, 60.2, 60.0, 42.6, 29.2. HR-MS m/z calculated for $\text{C}_{18}\text{H}_{22}\text{FN}_6\text{O}_2\text{S}$: 373.1783 [M + H] $^+$, found 373.1794 [M + H] $^+$.

4.1.20. 3-(4-amino-1-(*tert*-butyl)-1*H*-pyrazolo[3,4-*d*]pyrimidin-3-yl)-*N*-cyclopropylbenzamide **25**

The product **25** was obtained as a pale yellow solid in 70 % yield (46 mg). ^1H NMR (500 MHz, DMSO) δ 8.53 (d, $J = 4.2$ Hz, 1H), 8.26 (s, 1H), 8.09 (s, 1H), 7.92 (d, $J = 7.8$ Hz, 1H), 7.77 (d, $J = 7.7$ Hz, 1H), 7.61 (t, $J = 7.7$ Hz, 1H), 2.89 (tq, $J = 7.9, 4.0$ Hz, 1H), 1.77 (s, 9H), 0.74 – 0.68 (m, 2H), 0.62 – 0.56 (m, 2H). ^{13}C NMR (126 MHz, DMSO) δ 167.6, 158.7, 155.2, 154.4, 141.7, 135.5, 133.7, 131.4, 129.4, 127.6, 127.6, 99.2,

60.2, 29.2, 23.6, 6.2. HR-MS m/z calculated for $C_{19}H_{23}N_6O$: 351.1928 $[M + H]^+$, found 351.1967 $[M + H]^+$.

4.1.21. 4-(4-amino-1-(tert-butyl)-1H-pyrazolo[3,4-d]pyrimidin-3-yl)-2,6-difluorophenol **26**

The product **26** was obtained as a yellow solid in 57 % yield (34 mg). 1H NMR (250 MHz, DMSO) δ 10.47 (s, 1H), 8.23 (s, 1H), 7.26 (dd, $J = 7.6, 1.6$ Hz, 2H), 6.89 (s, 2H), 1.74 (s, 9H). ^{13}C NMR (126 MHz, DMSO) δ 158.2, 154.7, 153.9, 153.4, 153.4, 151.5, 151.4, 140.0, 134.2, 134.1, 134.0, 123.6, 123.5, 123.4, 112.1, 112.0, 112.0, 111.9, 98.6, 59.7, 28.7. HR-MS m/z calculated for $C_{15}H_{16}F_2N_5O$: 320.1317 $[M + H]^+$, found 320.1343 $[M + H]^+$.

4.2. Protein production and purification

The sequence for MKK3 (residues G53 to E345, NP_001303261.1) with S198E/T193E mutations inserted by site-directed mutagenesis was cloned into a pFB-GST3C-LIC vector, which confers an N-terminal GST tag, using LIC cloning. The plasmid was transformed into DH10Bac competent cells to generate bacmid DNA and this was later used to transfect Sf9 insect cells using Cellfectin (Thermo Fisher). Briefly, 1 mL of Sf9 cells at 2×10^5 cells/mL was added to a 24-well plate and incubated for 1 h at 27 °C to allow cell attachment. A transfection mix was prepared using Grace's insect medium (Thermo Fisher), the bacmid DNA, and Cellfectin. This mix was added to the attached cells and incubated for 5 h at 27 °C. After that, the transfection mix was removed and 0.8 mL of fresh Sf900-II medium containing 2 % FBS and 0.1 % Penicillin-Streptomycin was added to each well. The plate was incubated for 96 h and the P0 supernatant virus was harvested by centrifugation for 20 min at 1500 x g. The P0 virus stock was used to transfect Sf9 cells at 2×10^6 cells/mL. The plate was incubated for 72 h and the P1 virus was harvested by centrifugation. The P1 virus stock was used to transfect 2 L of Sf9 cells. After 72 h, cells were pelleted and resuspended in cold lysis buffer (50 mM HEPES pH 7.5, 300 mM NaCl, 10 % glycerol, and 1 mM TCEP) containing protease inhibitor cocktail III (Melford). Cells were disrupted by sonication using Vibra Cell sonicator (Sonics) for 3 min on ice (5 s on / 10 s off; amplitude = 35 %). Lysed cells were centrifuged for 45 min at 40,000g at 4 °C. The cell lysate was applied to a glutathione resin equilibrated with lysis buffer. After washing steps, purified MKK3E was eluted using the same buffer with the addition of 10 mM glutathione. Purification was confirmed by SDS-PAGE (Fig. 1A) and identity was confirmed by intact protein mass spectrometry.

4.3. MKK3E enzymatic activity

Constitutively active MKK3E enzymatic activity was measured using the Cisbio TR-FRET KinEASE kit. Measurement of $K_{M,ATP}$ was executed using 100 nM enzyme, 1 μ M of peptide STK-3-biotin and varying ATP concentrations (the highest concentration used was 200 μ M), and 90 min incubation at 30 °C. Time courses to ensure reaction linearity were run for up to 3 h using ATP at two different concentrations (1 and 2 μ M). Enzyme EC_{50} and EC_{80} were calculated using 100 μ M ATP, 1 μ M S3 peptide, and varying MKK3E concentrations, starting at 400 nM and using 2-fold serial dilutions.

To test the inhibitors, a mixture of 100 nM MKK3E and varying compound concentrations was incubated for 30 min at room temperature. After, the ATP (1 μ M) and STK-3-biotin (1 μ M) were added, the reaction was allowed to proceed for at least 90 min. The reaction was stopped with the addition of antibody-EU and streptavidin-XL665 diluted in the detection buffer. All data fitting was done in GraphPad Prism 9.

4.4. Molecular docking and dynamics

MKK3 was cloud-server constructed using SWISS-MODELL (<https://swissmodel.expasy.org/>)^{60–63}. The crystal structure of MKK7

(PDB ID: 6IB2; 42 % sequence identity to MKK3) was used as template for homology modelling and the resulting MKK3 model was used for rigid docking. The crystal structure of **2** bound to human mTOR kinase (PDB ID: 4JT5) was used to set the pose for **2**. The compound was manually extracted and docked into the MKK3 model, using Pymol. Compound **2** was exported to the Automated Topology Builder server (<https://atb.uq.edu.au/>)^{64–66} for the generation of input parameters for molecular dynamics. The coordinates were used to set a complex composed of the MKK3 and **2** in Gromacs (2021.4-plumed-2.7.3). The complex was solvated (12473 SPC water molecules) and ions were added to neutralize the system (6Na⁺ ions). The solvated system was minimized by 50,000 steps of steepest descent. The Verlet cutoff scheme, the Bussi–Parrinello thermostat LINCS for the constraints (all bonds), and the particle mesh Ewald for electrostatics, with a short-range cutoff of 12 Å, were applied. The system was equilibrated in two subsequent steps: 100 ps in NVT ensemble at 300 K, and 100 ps in NPT ensemble. In the equilibration steps, harmonic positional restraints were applied on the backbone of the protein and the heavy atoms of the ligand with a spring constant of 1000 kJ/(mol·Å²). The integration step was set to 2 fs. Finally, a 100 ns MD run was performed without constraints. Gromacs rmsd was used to determine the heavy atom drift along the simulation regarding the original position (last step of energy minimization). The calculated parameters were exported to GraphPad Prism 9 for graph construction. Pymol (v. 2.5.2) was used for visualization of the MD.

The structure of MKK bond to **2** was employed to generate a docking pose for compound **26**. First, the ligand–protein complex was extracted using Pymol and were prepared using Maestro (v. 12.9.137, Schrödinger 2023–3). Compound **26** was constructed and was energy minimized using ligprep module available in Maestro. The optimized structure was used for docking at MKK3 using **2** as a template. The reported pose was energy minimized using the “Refine Protein-Ligand Complex” tool available in the Schrödinger Prime module for protein atoms within a 5 Å radius of ligand atoms in the docked structure. Then, all atoms in both protein–ligand complexes were energy-minimized using the Monte Carlo sampling algorithm. The final minimized complex was used for MD simulations using Gromacs, under the same conditions described before for **2**. Gromacs rmsd was used to determine the heavy atom drift along the simulation regarding the original position (Fig. S8A). The trajectory between 20 and 100 ns was extracted and used for clustering according to the binding site RMSD using Gromacs cluster with a cutoff of 0.15 nm. Thirty-nine clusters were obtained, and each of them was represented by a centroid reference structure (Fig. S8B). The representative structure from the most populated cluster was then exported for visualization (Fig. S8C). The calculated RMSD parameters were exported to GraphPad Prism 9 for graph construction. Pymol (v. 2.5.2) was used for visualization of the MD.

4.5. BRET assay

BRET assays were performed as described previously^{26,67} using a plasmid encoding full-length MKK3 fused in-frame to nanoLuc (C-terminal) - a kind gift from Promega Corporation. Briefly, HEK293T cells were maintained in DMEM supplemented with 10 % fetal bovine serum (FBS) with 1 % penicillin and streptomycin. At day 1, cells were transfected with a mix containing 10 μ g of plasmid and 30 μ L of FUGENE in 1 mL Opti-MEM serum-free medium (Life Technologies). Prior to transfection, this mixture was kept at room temperature for 15 min. The transfection mix was added to the 3×10^6 cells plated on a 100 mm petri dish, then kept in an incubator at 37 °C, under 5 % CO₂, for 48 h. At day 3, cells were washed, detached (trypsinized), and counted. Cell medium was changed to Opti-MEM and cell density was adjusted to 2×10^5 cells/mL. A volume of 85 μ L of cells was transferred to each well in a 96-wells white plate (Greiner Bio-One, 655098). Tracer K-9 (Promega, N2632; in DMSO-D₆) was diluted in buffer containing 32.2 % PEG₄₀₀, 12.5 mM HEPES pH 7.5 at a ratio of 1:4. A volume of 5 μ L of the diluted tracer was added to each of the wells containing 85 μ L of cells in the assays plate.

Final tracer concentration was 1.0 μM . Compounds were first serially diluted in DMSO- D_6 , then Opti-MEM was added to 10x the final assay concentration. A volume of 10 μL of 10x compound was added to each well containing cells and tracer in the assay plate (final DMSO- D_6 concentration was 2 %). The assay plate was incubated for 2 h, and a detection mixture containing nLuc substrate and inhibitor (Promega, Cat. N2162) diluted in Opti-MEM was added to wells containing cells. Light emissions at 460 + 10 nm (BRET donor) and at 610 + 20 nm (BRET acceptor) were sequentially recorded (integration time = 0.5 s, gain = 3600) using a luminometer (BMG LABTECH CLARIOstar). Raw BRET values were calculated by dividing the acceptor fluorescence (620 nm) by the donor luminescence (450 nm) signals. These are reported as milli-BRET (mBRET) units (mBU), according to Eq. (1):

$$mBRET(mBU) = \left(\frac{\text{Acceptor}_{\text{sample}}}{\text{Donor}_{\text{sample}}} \right) \times 1,000 \quad (1)$$

BRET values were converted to blank-corrected, normalized BRET (%) according to Eq. (2):

$$\text{NormalizedBRET}(\%) = \frac{X - Z}{Y - Z} \times 100 \quad (2)$$

Where X = mBRET value in the presence of the test compound and the probe, Y = mBRET value in the presence of probe only, and Z = mBRET value in the absence of probe and test compound.

4.6. Human kinase panel

The 28 proteins present in the selectivity panels were produced using plasmid pNIC-Bio3 (*E. coli*) or pFB-Bio5 (insect cells). These vectors contain a C-terminus Avi-tag sequence for lysine biotinylation (GLNDI-FEAQKIEWHE). For the expression in *E. coli*, the target kinases were co-expressed with BirA biotin ligase previously cloned into the plasmid pCDF-BirA, which confers resistance to spectinomycin. For Sf9 cells, the biotinylation was performed by a secreted BirA which is co-expressed along with the target kinase. In both expression systems, 0.14 mM biotin (final concentration) was added to cell media together with IPTG for *E. coli* or during baculovirus infection for Sf9 cells. Protein biotinylation was confirmed by intact mass analysis using mass spectrometry - biotinylated targets display an increase of 226.31 Da in their molecular mass. Protein kinases tagged with biotin were incubated for an hour at room temperature with 0.6 nM Eu-Streptavidin (Thermo Fisher, Cat. PV6025), a tracer containing Alexa Fluor-647 and the inhibitor to be tested. Binding of the tracer to the kinase ATP pocket results in a high TR-FRET signal (excitation at 340 nm and emission at 665/615 nm). Competitive displacement of the tracer by test compounds decreases the TR-FRET signal. Tracers used were T236, T178, T199, and T222 sourced from Thermo Fischer Scientific. Proteins were at 15 nM, compounds **2** and **26** at 1 μM , and control inhibitors at 10 μM (Staurosporine for T222 and T236, Dasatinib for T178, SB-202190 for T199). Protein kinases, tracer identities and their concentration can be found in Table S2. Displacement of 0 % was calculated using DMSO and 100 % using the described inhibitor for each protein.

CRedit authorship contribution statement

Jéssica E. Takarada: Methodology, Formal analysis, Investigation, Writing – original draft, Writing – review & editing, Conceptualization. **Micael R. Cunha:** Conceptualization, Formal analysis, Investigation, Methodology, Writing – original draft, Writing – review & editing. **Vitor M. Almeida:** Conceptualization, Investigation, Methodology, Writing – original draft, Writing – review & editing. **Stanley N.S. Vasconcelos:** Conceptualization, Formal analysis, Methodology. **André S. Santiago:** Formal analysis, Investigation, Methodology. **Paulo H. Godoi:** Conceptualization, Formal analysis, Methodology, Validation. **Anita Salmazo:** Methodology. **Priscila Z. Ramos:** Methodology. **Angela M. Fala:** Methodology. **Lucas R. de Souza:** Investigation. **Italo E.P. Da**

Silva: Methodology. **Mario H. Bengtson:** Funding acquisition, Writing – review & editing. **Katlin B. Massirer:** Funding acquisition, Writing – review & editing. **Rafael M. Couñago:** Conceptualization, Formal analysis, Funding acquisition, Supervision, Writing – review & editing.

Declaration of competing interest

The authors declare that they have no known competing financial interests or personal relationships that could have appeared to influence the work reported in this paper.

Data availability

Data will be made available on request.

Acknowledgments

We thank all members of CQMED-UNICAMP for their help and support. We thank the staff of the Life Sciences Core Facility (LaCTAD) at UNICAMP for the Genomics analysis. We thank the NMR facility at UNICAMP Chemistry Institute for its assistance. This work was supported by FAPESP (Fundação de Amparo à Pesquisa do Estado de São Paulo) (grant # 2014/50897-0), Embrapii (Empresa Brasileira de Pesquisa e Inovação Industrial), CNPq (Conselho Nacional de Desenvolvimento Científico e Tecnológico) (grant # 465651/2014-3). J.E.T., A.M. F, P.Z.R and I.E.P.S were the recipient of fellowships from the Coordenação de Aperfeiçoamento de Pessoal de Nível Superior, CAPES (grant #s 88887.373547/2019-00, 88887.136437/2017-00, 88887.136432/2017-00 and 88887.373111/2019-00, respectively). S.N.S.V, L.R.S, M. R.C. and V.M.A. were recipients of fellowships from the Fundação de Amparo à Pesquisa do Estado de São Paulo, FAPESP (grant #s. 2018/09475-5, 2020/16094-8, 2021/04853-4 and 2022/00743-2, respectively).

Appendix A. Supplementary material

Supplementary data to this article can be found online at <https://doi.org/10.1016/j.bmc.2023.117561>.

References

- Roux PP, Blenis J. ERK and p38 MAPK-activated protein kinases: a family of protein kinases with diverse biological functions. *Microbiol Mol Biol Rev*. 2004;68:320–344. <https://doi.org/10.1128/MMBR.68.2.320-344.2004>.
- Akinleye A, Furqan M, Mukhi N, Ravella P, Liu D. MEK and the inhibitors: from bench to bedside. *J Hematol Oncol*. 2013;6:27. <https://doi.org/10.1186/1756-8722-6-27>.
- Cargnello M, Roux PP. Activation and Function of the MAPKs and Their Substrates, the MAPK-Activated Protein Kinases. *Microbiol Mol Biol Rev*. 2011;75:50–83. <https://doi.org/10.1128/MMBR.00031-10>.
- Kim EK, Choi EJ. Pathological roles of MAPK signaling pathways in human diseases. *Biochimica et Biophysica Acta (BBA) - Molecular Basis of Disease*. 2010;1802:396–405. <https://doi.org/10.1016/j.bbdis.2009.12.009>.
- Wagner EF, Nebreda ÁR. Signal integration by JNK and p38 MAPK pathways in cancer development. *Nat Rev Cancer*. 2009;9:537–549. <https://doi.org/10.1038/nrc2694>.
- Kong TT, Zhang CM, Liu ZP. Recent Developments of p38 α MAP Kinase Inhibitors as Antiinflammatory Agents Based on the Imidazole Scaffolds. *CMC*. 2013;20:1997–2016. <https://doi.org/10.2174/0929867311320150006>.
- Peifer C, Wagner G, Laufer S. New approaches to the treatment of inflammatory disorders small molecule inhibitors of p38 MAP Kinase. *CTMC*. 2006;6:113–149. <https://doi.org/10.2174/156802606775270323>.
- Goldstein D, Gabriel T. Pathway to the clinic: inhibition of P38 MAP kinase. A review of ten chemotypes selected for development. *CTMC*. 2005;5:1017–1029. <https://doi.org/10.2174/1568026054985939>.
- Haller V, Nahidino P, Forster M, Laufer SA. An updated patent review of p38 MAP kinase inhibitors (2014–2019). *Expert Opin Ther Pat*. 2020;30:453–466. <https://doi.org/10.1080/13543776.2020.1749263>.
- Martínez-Limón A, Joaquín M, Caballero M, Posas F, de Nadal E. The p38 pathway: from biology to cancer therapy. *IJMS*. 2020;21:1913. <https://doi.org/10.3390/ijms21061913>.

11. Shin I, Kim S, Song H, Kim HRC, Moon A. H-Ras-specific Activation of Rac-MKK3/6-p38 Pathway. *J Biol Chem*. 2005;280:14675–14683. <https://doi.org/10.1074/jbc.M411625200>.
12. Jin K, Lim S, Mercer SE, Friedman E. The Survival Kinase Mirk/dyrk1B Is Activated through Rac1-MKK3 Signaling. *J Biol Chem*. 2005;280:42097–42105. <https://doi.org/10.1074/jbc.M507301200>.
13. Stramucci L, Pranteda A, Stravato A, et al. MKK3 sustains cell proliferation and survival through p38DELTA MAPK activation in colorectal cancer. *Cell Death Dis*. 2019;10:842. <https://doi.org/10.1038/s41419-019-2083-2>.
14. Baldari S, Ubertini V, Garufi A, D'Orazi G, Bossi G. Targeting MKK3 as a novel anticancer strategy: molecular mechanisms and therapeutic implications. *Cell Death Dis*. 2015;6:e1621–e. <https://doi.org/10.1038/cddis.2014.591>.
15. Adams M, Kobayashi T, Lawson JD, et al. Fragment-based drug discovery of potent and selective MKK3/6 inhibitors. *Bioorg Med Chem Lett*. 2016;26:1086–1089. <https://doi.org/10.1016/j.bmcl.2015.11.054>.
16. Tibbles LA, Ing YL, Kiefer F, et al. MLK-3 activates the SAPK/JNK and p38/RK pathways via SEK1 and MKK3/6. *EMBO J*. 1996;15:7026–7035. <https://doi.org/10.1002/j.1460-2075.1996.tb01094.x>.
17. Raingeaud J, Whitmarsh AJ, Barrett T, Dérjard B, Davis RJ. MKK3- and MKK6-regulated gene expression is mediated by the p38 mitogen-activated protein kinase signal transduction pathway. *Mol Cell Biol*. 1996;16:1247–1255. <https://doi.org/10.1128/MCB.16.3.1247>.
18. Juyoux P, Galdadas I, Gobbo D, et al. Architecture of the MKK6-p38 α complex defines the basis of MAPK specificity and activation. *Science*. 2023;381:1217–1225. <https://doi.org/10.1126/science.add7859>.
19. Deibler KK, Mishra RK, Clutter MR, et al. A Chemical Probe Strategy for Interrogating Inhibitor Selectivity Across the MEK Kinase Family. *ACS Chem Biol*. 2017;12:1245–1256. <https://doi.org/10.1021/acscchembio.6b01060>.
20. Cho H, Sengupta S, Jeon SSH, et al. Identification of the First Selective Activin Receptor-Like Kinase 1 Inhibitor, a Reversible Version of L-783277. *J Med Chem*. 2017;60:1495–1508. <https://doi.org/10.1021/acs.jmedchem.6b01679>.
21. Zhang JH, Chung TDY, Oldenburg KR. A Simple Statistical Parameter for Use in Evaluation and Validation of High Throughput Screening Assays. *SLAS Discovery*. 1999;4:67–73. <https://doi.org/10.1177/108705719900400206>.
22. Gribble FM, Loussouarn G, Tucker SJ, Zhao C, Nichols CG, Ashcroft FM. A Novel Method for Measurement of Submembrane ATP Concentration. *J Biol Chem*. 2000;275:30046–30049. <https://doi.org/10.1074/jbc.M001010200>.
23. Wells C, Couñago RM, Limas JC, et al. SGC-AAK1-1: A Chemical Probe Targeting AAK1 and BMP2K. *ACS Med Chem Lett*. 2020;11:340–345. <https://doi.org/10.1021/acmedchemlett.9b00399>.
24. Agajanian MJ, Walker MP, Axtman AD, et al. WNT Activates the AAK1 Kinase to Promote Clathrin-Mediated Endocytosis of LRP6 and Establish a Negative Feedback Loop. *Cell Rep*. 2019;26:79–93.e8. <https://doi.org/10.1016/j.celrep.2018.12.023>.
25. Hall MP, Unch J, Binkowski BF, et al. Engineered Luciferase Reporter from a Deep Sea Shrimp Utilizing a Novel Imidazopyridine Substrate. *ACS Chem Biol*. 2012;7:1848–1857. <https://doi.org/10.1021/cb3002478>.
26. Vasta JD, Corona CR, Wilkinson J, et al. Quantitative, Wide-Spectrum Kinase Profiling in Live Cells for Assessing the Effect of Cellular ATP on Target Engagement. *Cell Chem Biol*. 2018;25:206–214.e11. <https://doi.org/10.1016/j.chembiol.2017.10.010>.
27. Liu Q, Thoreen C, Wang J, Sabatini D, Gray NS. mTOR mediated anti-cancer drug discovery. *Drug Discovery Today: Therapeutic Strategies*. 2009;6:47–55. <https://doi.org/10.1016/j.ddstr.2009.12.001>.
28. Hsieh AC, Liu Y, Edlind MP, et al. The translational landscape of mTOR signalling steers cancer initiation and metastasis. *Nature*. 2012;485:55–61. <https://doi.org/10.1038/nature10912>.
29. Apse B, Blair JA, Gonzalez B, et al. Targeted polypharmacology: discovery of dual inhibitors of tyrosine and phosphoinositide kinases. *Nat Chem Biol*. 2008;4:691–699. <https://doi.org/10.1038/nchembio.117>.
30. Bartscht T, Lehnert H, Gieseler F, Ungefroren H. The Src family kinase inhibitors PP2 and PP1 effectively block TGF-beta1-induced cell migration and invasion in both established and primary carcinoma cells. *Cancer Chemother Pharmacol*. 2012;70:221–230. <https://doi.org/10.1007/s00280-012-1904-0>.
31. Bishop AC, Kung C yun, Shah K, Witucki L, Shokat KM, Liu Y. Generation of Monospecific Nanomolar Tyrosine Kinase Inhibitors via a Chemical Genetic Approach. *J Am Chem Soc*. 1999;121(4):627–631. doi:10.1021/ja983267v.
32. Verschuere K, Cobbaut M, Demaerel J, et al. Discovery of a potent protein kinase D inhibitor: insights in the binding mode of pyrazolo[3,4-d]pyrimidine analogues. *Med Chem Commun*. 2017;8:640–646. <https://doi.org/10.1039/C6MD00675B>.
33. Tandon M, Johnson J, Li Z, Xu S, Wipf P, Wang QJ. New Pyrazolopyrimidine Inhibitors of Protein Kinase D as Potent Anticancer Agents for Prostate Cancer Cells. *Kanzaki M, ed. PLoS ONE*. 2013;8(9):e75601. doi:10.1371/journal.pone.0075601.
34. Sun SY. mTOR kinase inhibitors as potential cancer therapeutic drugs. *Cancer Lett*. 2013;340:1–8. <https://doi.org/10.1016/j.canlet.2013.06.017>.
35. Machova Urdzikova L, Cimermanova V, Karova K, et al. The Role of Green Tea Catechin Epigallocatechin Gallate (EGCG) and Mammalian Target of Rapamycin (mTOR) Inhibitor PP242 (Torkinib) in the Treatment of Spinal Cord Injury. *Antioxidants*. 2023;12:363. <https://doi.org/10.3390/antiox12020363>.
36. Zhou K, Chen X, Zhang L, et al. Targeting peripheral immune organs with self-assembling prodrug nanoparticles ameliorates allogeneic heart transplant rejection. *Am J Transplant*. 2021;21:3871–3882. <https://doi.org/10.1111/ajt.16748>.
37. Yang H, Rudge DG, Koos JD, Vaidialingam B, Yang HJ, Pavletich NP. mTOR kinase structure, mechanism and regulation. *Nature*. 2013;497:217–223. <https://doi.org/10.1038/nature12122>.
38. Jumper J, Evans R, Pritzel A, et al. Highly accurate protein structure prediction with AlphaFold. *Nature*. 2021;596:583–589. <https://doi.org/10.1038/s41586-021-03819-2>.
39. Matsumoto T, Kinoshita T, Matsuzaka H, et al. Crystal structure of non-phosphorylated MAP2K6 in a putative auto-inhibition state. *J Biochem*. 2012;151:541–549. <https://doi.org/10.1093/jb/mvs023>.
40. Min X, Akella R, He H, et al. The Structure of the MAP2K MEK6 Reveals an Autoinhibitory Dimer. *Structure*. 2009;17:96–104. <https://doi.org/10.1016/j.str.2008.11.007>.
41. Defnet A, Martínez R, Shapiro P. Protein Kinase Interactions with Regulatory and Effector Proteins. In: Shapiro P, ed. *Next Generation Kinase Inhibitors*. Springer International Publishing; 2020:61–80. https://doi.org/10.1007/978-3-030-48283-1_4.
42. Jain R, Mathur M, Lan J, et al. Discovery of Potent and Selective RSK Inhibitors as Biological Probes. *J Med Chem*. 2015;58:6766–6783. <https://doi.org/10.1021/acs.jmedchem.5b00450>.
43. Lackey K, Cory M, Davis R, et al. The discovery of potent cRaf1 kinase inhibitors. *Bioorg Med Chem Lett*. 2000;10:223–226. [https://doi.org/10.1016/S0960-894X\(99\)00668-X](https://doi.org/10.1016/S0960-894X(99)00668-X).
44. Serafim RAM, De Souza Gama FH, Dutra LA, et al. Development of Pyridine-based Inhibitors for the Human Vaccinia-related Kinases 1 and 2. *ACS Med Chem Lett*. 2019;10:1266–1271. <https://doi.org/10.1021/acsmchemlett.9b00082>.
45. Couñago RM, Allerston CK, Savitsky P, et al. Structural characterization of human Vaccinia-Related Kinases (VRK) bound to small-molecule inhibitors identifies different P-loop conformations. *Sci Rep*. 2017;7:7501. <https://doi.org/10.1038/s41598-017-07755-y>.
46. Baillache DJ, Unciti-Broceta A. Recent developments in anticancer kinase inhibitors based on the pyrazolo[3,4-d]pyrimidine scaffold. *RSC Med Chem*. 2020;11:1112–1135. <https://doi.org/10.1039/D0MD000227E>.
47. Schenone S, Radi M, Musumeci F, Brullo C, Botta M. Biologically Driven Synthesis of Pyrazolo[3,4-d]pyrimidines As Protein Kinase Inhibitors: An Old Scaffold As a New Tool for Medicinal Chemistry and Chemical Biology Studies. *Chem Rev*. 2014;114:7189–7238. <https://doi.org/10.1021/cr400270z>.
48. Hopkins AL, Keserü GM, Leeson PD, Rees DC, Reynolds CH. The role of ligand efficiency metrics in drug discovery. *Nat Rev Drug Discov*. 2014;13:105–121. <https://doi.org/10.1038/nrd4163>.
49. Hopkins AL, Groom CR, Alex A. Ligand efficiency: a useful metric for lead selection. *Drug Discov Today*. 2004;9:430–431. [https://doi.org/10.1016/S1359-6446\(04\)03069-7](https://doi.org/10.1016/S1359-6446(04)03069-7).
50. Kenny PW. The nature of ligand efficiency. *J Cheminform*. 2019;11:8. <https://doi.org/10.1186/s13321-019-0330-2>.
51. Tarcsay Á, Nyíri K, Keserü GM. Impact of Lipophilic Efficiency on Compound Quality. *J Med Chem*. 2012;55:1252–1260. <https://doi.org/10.1021/jm201388p>.
52. Leeson PD, Bento AP, Gaulton A, et al. Target-Based Evaluation of “Drug-Like” Properties and Ligand Efficiencies. *J Med Chem*. 2021;64:7210–7230. <https://doi.org/10.1021/acs.jmedchem.1c00416>.
53. Johnson TW, Gallego RA, Edwards MP. Lipophilic Efficiency as an Important Metric in Drug Design. *J Med Chem*. 2018;61:6401–6420. <https://doi.org/10.1021/acs.jmedchem.8b00077>.
54. Chrienova Z, Rysanek D, Oleksak P, et al. Discovery of small molecule mechanistic target of rapamycin inhibitors as anti-aging and anti-cancer therapeutics. *Front Aging Neurosci*. 2022;14:1048260. <https://doi.org/10.3389/fnagi.2022.1048260>.
55. Manning G, Whyte DB, Martinez R, Hunter T, Sudarsanam S. The Protein Kinase Complement of the Human Genome. *Science*. 2002;298:1912–1934. <https://doi.org/10.1126/science.1075762>.
56. Liu Q, Kirubakaran S, Hur W, et al. Kinome-wide Selectivity Profiling of ATP-competitive Mammalian Target of Rapamycin (mTOR) Inhibitors and Characterization of Their Binding Kinetics. *J Biol Chem*. 2012;287:9742–9752. <https://doi.org/10.1074/jbc.M111.304485>.
57. Gilles P, Kashyap RS, Freitas MJ, et al. Design, synthesis and biological evaluation of pyrazolo[3,4-d]pyrimidine-based protein kinase D inhibitors. *Eur J Med Chem*. 2020;205:112638. <https://doi.org/10.1016/j.ejmech.2020.112638>.
58. Rutaganira FU, Barks J, Dhason MS, et al. Inhibition of Calcium Dependent Protein Kinase 1 (CDPK1) by Pyrazolopyrimidine Analogs Decreases Establishment and Recurrence of Central Nervous System Disease by *Toxoplasma gondii*. *J Med Chem*. 2017;60:9976–9989. <https://doi.org/10.1021/acs.jmedchem.7b01192>.
59. Todorovic N, Awuah E, Shakya T, Wright GD, Capretta A. Microwave-assisted synthesis of N1- and C3-substituted pyrazolo[3,4-d]pyrimidine libraries. *Tetrahedron Lett*. 2011;52:5761–5763. <https://doi.org/10.1016/j.tetlet.2011.08.103>.
60. Waterhouse A, Bertoni M, Bienert S, et al. SWISS-MODEL: homology modelling of protein structures and complexes. *Nucleic Acids Res*. 2018;46:W296–W303. <https://doi.org/10.1093/nar/gky427>.
61. Bienert S, Waterhouse A, de Beer TAP, et al. The SWISS-MODEL Repository—new features and functionality. *Nucleic Acids Res*. 2017;45:D313–D319. <https://doi.org/10.1093/nar/gkw1132>.
62. Guex N, Peitsch MC, Schwede T. Automated comparative protein structure modeling with SWISS-MODEL and Swiss-PdbViewer: A historical perspective. *Electrophoresis*. 2009;30:S162–S173. <https://doi.org/10.1002/elps.200900140>.
63. Studer G, Rempfer C, Waterhouse AM, Gumienny R, Haas J, Schwede T. QMEANDisCo—distance constraints applied on model quality estimation. Elofsson A, ed. *Bioinformatics*. 2020;36(6):1765–1771. doi:10.1093/bioinformatics/btz828.
64. Malde AK, Zuo L, Breeze M, et al. An Automated Force Field Topology Builder (ATB) and Repository: Version 1.0. *J Chem Theory Comput*. 2011;7:4026–4037. <https://doi.org/10.1021/ct200196m>.
65. Stroet M, Caron B, Visscher KM, Geerke DP, Malde AK, Mark AE. Automated Topology Builder Version 3.0: Prediction of Solvation Free Enthalpies in Water and

- Hexane. *J Chem Theory Comput.* 2018;14:5834–5845. <https://doi.org/10.1021/acs.jctc.8b00768>.
66. Gunsteren WF, Daura X, Fuchs PFJ, et al. On the Effect of the Various Assumptions and Approximations used in Molecular Simulations on the Properties of Bio-
- Molecular Systems: Overview and Perspective on Issues. *ChemPhysChem.* 2021;22: 264–282. <https://doi.org/10.1002/cphc.202000968>.
67. Berger BT, Amaral M, Kokh DB, et al. Structure-kinetic relationship reveals the mechanism of selectivity of FAK inhibitors over PYK2. *Cell Chem Biol.* 2021;28: 686–698.e7. <https://doi.org/10.1016/j.chembiol.2021.01.003>.